Nucleon-nucleon momentum-correlation function as a probe of the density distribution of valence neutrons in neutron-rich nuclei

X. G. Cao (曹喜光),[1] X. Z. Cai (蔡翔舟),[1,*] Y. G. Ma (马余刚),[1,†] D. Q. Fang (方德清),[1] G. Q. Zhang (张国强),[1] W. Guo (郭威),[1] J. G. Chen (陈金根),[1] and J. S. Wang (王建松)[2]

[1]*Shanghai Institute of Applied Physics, Chinese Academy of Sciences, Shanghai 201800, China*

[2]*Institute of Modern Physics, Chinese Academy of Sciences, Lanzhou 730000, China*

(Received 27 November 2011; revised manuscript received 24 July 2012; published 18 October 2012)

Proton-neutron, neutron-neutron, and proton-proton momentum-correlation functions (C_{pn}, C_{nn}, and C_{pp}) are systematically investigated for ^{15}C and other C-isotope-induced collisions at different entrance channel conditions within the framework of the isospin-dependent quantum-molecular-dynamics model complemented by the correlation after burner (CRAB) computation code. ^{15}C is a prime exotic nucleus candidate due to the weakly bound valence neutron coupling with closed-neutron-shell nucleus ^{14}C. To study density dependence of the correlation function by removing the isospin effect, the initialized ^{15}C projectiles are sampled from two kinds of density distribution from the relativistic mean-field (RMF) model in which the valence neutron of ^{15}C is populated in both $1d5/2$ and $2s1/2$ states, respectively. The results show that the density distributions of the valence neutron significantly influence the nucleon-nucleon momentum-correlation function at large impact parameters and high incident energies. The extended density distribution of the valence neutron largely weakens the strength of the correlation function. The size of the emission source is extracted by fitting the correlation function by using the Gaussian source method. The emission source size as well as the size of the final-state phase space are larger for projectile samplings from more extended density distributions of the valence neutron, which corresponds to the $2s1/2$ state in the RMF model. Therefore, the nucleon-nucleon momentum-correlation function can be considered as a potentially valuable tool to diagnose exotic nuclear structures, such as the skin and halo.

DOI: 10.1103/PhysRevC.86.044620 PACS number(s): 25.60.−t, 25.70.Pq, 21.10.Gv

I. INTRODUCTION

The intensity interferometry method, developed by Hanbury Brown and Twiss (HBT) in the 1950s [1], was originally used to measure astronomical objects, such as the angular diameter of stars. The method was later introduced into subatomic physics by Goldhaber *et al*., who extracted the spatial extent of an annihilation fireball in proton-antiproton reactions by two-pion correlations [2]. Then, the method was widely applied in exploring the nuclear reactions from low energy to relativistic energy [3–10]. Recently, it has been extended to other fields, for instance, the analogous correlations that describe the fermionic statics of elections [11,12].

In heavy-ion collisions (HICs) at intermediate energy, the HBT method is widely used to extract the space-time properties, such as the source size and emission time of fragments by two-particle correlation functions [13,14]. The dependences of the momentum-correlation function on the impact parameter [15,16], the total momentum of nucleon pairs [16,17], the isospin of the emitting source [18], the nuclear symmetry energy [19], and the nuclear equation of state (EOS) [16] are also explored by experiment and theory.

Besides the applications of two-particle momentum-correlation functions to investigate the heavy-ion collision process, the HBT method is also extended to study the exotic structure of nuclei far from the β-stability line due to the rapid development of radioactive nuclear beams. The neutron-neutron correlation functions (C_{nn}) of Borromean halo nuclei, such as ^{6}He, ^{11}Li, and ^{14}Be are constructed to extract the size of separation between the two halo neutrons [20–25]. In addition, Ma *et al*. [16] and Wei *et al*. [26,27] found that the strength of the proton-neutron momentum-correlation functions at small relative momentum has a linear dependence on the binding energy per nucleon or single-neutron separation energy for light isotope chains. The analogous suppressed proton-proton correlation function is also suggested as another potential tool to diagnose proton-halo nuclei [28] besides the conventional methods, such as total reaction cross section and momentum distribution width measurements [29,30]. Ma *et al*. [31,32] have carried out an experiment on the Rikagaku Kenkyusho (RIKEN) Projectile Fragment Separator at RIKEN to measure the proton-proton momentum-correlation function for revealing the exotic structure of the proton-rich nucleus ^{23}Al. Therefore, it is very interesting to investigate how the exotic structure affects the nucleon-nucleon (NN) momentum-correlation function, which can serve as a potential observable to extract information about anomalous structures in a nuclei.

In this paper, we calculated $^{15}\mathrm{C} + {}^{12}\mathrm{C}$ collisions with the isospin-dependent quantum-molecular-dynamics (IDQMD) model. ^{15}C is a one-neutron-halo candidate because of its small neutron separation energy: $S_n = 1.218$ MeV [33], closed-neutron-shell core: ^{14}C, narrower momentum distribution of the ^{14}C fragment from the breakup of ^{15}C [34,35], and a larger s-wave spectroscopic factor of the ^{15}C ground state [36] by the $^{14}\mathrm{C}(d,p)^{15}\mathrm{C}$ reaction measurement. However, a consistent picture has not been obtained in the reaction cross-sectional

*caixz@sinap.ac.cn
†ygma@sinap.ac.cn

measurement. The interaction cross section (σ_I) does not have a peculiarity compared with neighbor isotopes at an incident energy of 740 MeV/nucleon [37]. However, the reaction cross section (σ_R), more or less, shows enhancement at intermediate energies, and there is also a large difference factor (d) for σ_R [35,38], which is defined as [39]: $d = \frac{\sigma_R(\mathrm{exp})-\sigma_R(G)}{\sigma_R(G)}$, where $\sigma_R(\mathrm{exp})$ represents intermediate-energy experimental σ_R and $\sigma_R(G)$ is the σ_R calculated by the Glauber model at the same bombarding energy with HO-type density distribution, which is obtained by fitting experimental σ_R at high energy. The s-wave spectroscopic factor extracted from σ_I is also different from the value obtained from the transfer reaction. Fang *et al.* found that the s-wave component is dominant in the ground state of ^{15}C by simultaneous measurement of σ_R and momentum distribution [35]. However, the fitted results by the Glauber model are deviated from the experimental data at low energies for σ_R. Therefore, new probes are needed to estimate the density distribution of the valence neutron in ^{15}C and other analogous neutron-rich exotic nucleus candidates.

The initialized ^{15}C projectiles are sampled from densities calculated by the relativistic mean-field (RMF) model to study how density distributions of the outer neutron affect the nucleon-nucleon momentum-correlation function. In the RMF model, the last neutron of ^{15}C is populated in both $1d5/2$ and $2s1/2$ states, respectively. Because the isospin degree of freedom is removed, the relationship between the momentum-correlation function and the structure of the exotic nuclei, such as skin can be more directly explored by comparing different collisions induced by different configured ^{15}C projectiles.

The rest of this paper is organized as follows: In Sec. II, we briefly describe the HBT technique and the IDQMD model; the initialization of ^{15}C projectiles and the nucleon-nucleon momentum-correlation function of different configured C-isotope-induced collisions are discussed in Sec. III; the summary is presented in Sec. IV.

II. HBT TECHNIQUE AND IDQMD MODEL

A. HBT technique

It is known that the final-state interaction (FSI) and quantum-statistical symmetry (QSS) affect the wave function of the relative motion of light identical particles when they are emitted in a close region in phase space and time, which is the principle of intensity interferometry, i.e., the HBT method. The correlation function of two particles can be obtained by convolution of the emission function $g(\mathbf{p}, x)$ in the standard *Koonin-Pratt* equation [3–5],

$$C(\mathbf{P}, \mathbf{q}) = \frac{\int d^4x_1 d^4x_2 g(\mathbf{P}/2, x_1) g(\mathbf{P}/2, x_2) |\phi(\mathbf{q}, \mathbf{r})|^2}{\int d^4x_1 g(\mathbf{P}/2, x_1) \int d^4x_2 g(\mathbf{P}/2, x_2)}, \quad (1)$$

where $\mathbf{P}(= \mathbf{p}_1 + \mathbf{p}_2)$ and $\mathbf{q}[= (\mathbf{p}_1 - \mathbf{p}_2)/2]$ are the total and relative momenta of the particle pair, respectively, $g(\mathbf{p}, x)$ is the probability of emitting a particle with momentum $\mathbf{p}$ at the space-time point $x(\mathbf{r}, t)$, and $\phi(\mathbf{q}, \mathbf{r})$ is the two-particle relative wave function with relative distance $\mathbf{r} = (\mathbf{r}_2 - \mathbf{r}_1) - \frac{1}{2}(\mathbf{v}_1 + \mathbf{v}_2)(t_2 - t_1)$.

In a specific application of the Koonin-Pratt formula, the reliable single-particle phase-space distribution at the freeze-out stage is needed [15]. In this paper, the IDQMD model is used as the event generator. It is a widely used transport model in intermediate-energy HICs and has been successfully applied to HBT studies for neutron-rich nuclei-induced reactions by Ma *et al.* [16,28], and Wei *et al.* [26,27]. The phase space of the emitted particles is used as the input of Pratt's correlation after burner (CRAB) code [40], which takes the FSI and QSS effects into account for remedying the disadvantage of the semiclassical transport model.

B. IDQMD model

The quantum-molecular-dynamics (QMD) approach is a many-body theory that can describe HICs from intermediate to relativistic energies [41–43]. The main advantage of the QMD model is that it can explicitly treat the many-body state of the collision system, so it contains correlation effects for all orders. Therefore, the QMD model provides valuable information about both the collision dynamics and the fragmentation process. The model also has excellent extensibility due to its microscopic treatment of the collision process. It mainly consists of several parts: initialization of the projectile and the target nucleons, propagation of nucleons in the effective potential, NN collisions in a nuclear medium, Pauli blocking, and the numerical test.

The IDQMD model is based on the QMD model and affiliates the isospin factors in mean-field, two-body NN collisions, and Pauli blocking [16,26,44–47]. In addition, the phase-space sampling of neutrons and protons in the initialization should be separately treated because of the large difference between neutron and proton density distributions for nuclei far from the β-stability line. To properly incorporate nuclear structure effects into microscopic simulations, stable initialized ^{15}C with and without a neutron-halo structure have been sampled.

In the IDQMD model, each nucleon is represented by a Gaussian wave packet with width $\sqrt{L}$ (here, $L = 2.16$ fm^2) centered around the mean position $\vec{r}_i(t)$ and the mean momentum $\vec{p}_i(t)$,

$$\psi_i(\vec{r}, t) = \frac{1}{(2\pi L)^{3/4}} \exp\left[-\frac{[\vec{r} - \vec{r}_i(t)]^2}{4L}\right] \exp\left[\frac{i\vec{r} \cdot \vec{p}_i(t)}{\hbar}\right]. \quad (2)$$

Then, all nucleons interact via mean-field and NN collisions. The nuclear mean field is parametrized by

$$U(\rho, \tau_z) = \alpha\left(\frac{\rho}{\rho_0}\right) + \beta\left(\frac{\rho}{\rho_0}\right)^{\gamma} + \frac{1}{2}(1 - \tau_z)V_c + C_{\mathrm{sym}}\frac{\rho_n - \rho_p}{\rho_0}\tau_z + U^{\mathrm{Yuk}}, \quad (3)$$

with $\rho_0 = 0.16$ fm^{-3} (the normal nuclear matter density). ρ, ρ_n, and ρ_p are the total, neutron, and proton densities, respectively. τ_z is the zth component of the isospin degree of freedom, which equals 1 or -1 for neutrons or protons, respectively. The coefficients α, β, and γ are parameters of

the nuclear EOS. $C_{\rm sym}$ is the symmetry-energy strength due to the difference between the neutron and the proton, which takes the value of 32 MeV. In this paper, $\alpha = -356$, $\beta = 303$ MeV, and $\gamma = 7/6$ are taken, which correspond to the so-called soft EOS with Ref. [42]. V_c is the Coulomb potential, and $U^{\rm Yuk}$ is the Yukawa (surface) potential, which has the following form:

$$U^{\rm Yuk} = \frac{V_y}{2m}\sum_{i\neq j}\frac{1}{r_{ij}}\exp(Lm^2)[\exp(-mr_{ij}) \times \mathrm{erfc}(\sqrt{L}m - r_{ij}/\sqrt{4L}) - \exp(mr_{ij}) \times \mathrm{erfc}(\sqrt{L}m + r_{ij}/\sqrt{4L})], \quad (4)$$

with $V_y = -0.0074$ GeV, $m = 1.25$ fm^{-1}, and $r_{ij} = |\vec{r}_i - \vec{r}_j|$ is the relative distance between two nucleons. The experimental parametrized NN cross section, which is energy and isospin dependent, is used.

The Pauli-blocking effect in the IDQMD model is also isospin dependent. The blocking of neutrons and protons is separately treated as follows: Each nucleon occupies a six-dimensional sphere with a volume of $\hbar^3/2$ in the phase space (by considering the spin degree of freedom), and we calculate the phase-space volume (V) of the scattered nucleons, which are occupied by the rest of the nucleons with the same isospin as that of the scattered ones. We then compare $2V/\hbar^3$ with a random number and decide whether the collision is blocked or not.

The time evolution of the colliding system is given by the generalized variational principle. Nuclear clusters are constructed by a coalescence model in which particles with relative momentum smaller than P_0 and relative distance smaller than R_0 are considered to belong to one cluster. The parameter set: $P_0 = 300$ MeV/c and $R_0 = 3.5$ fm is taken here.

III. THE INITIALIZATION OF ^{15}C PROJECTILES AND SYSTEMATICAL HBT RESULTS

In IDQMD, the initialization of the projectiles targets distinct protons from neutrons. We sample the nucleon's coordinates from density distributions of protons and neutrons, which are calculated by the RMF method. Figure 1 shows

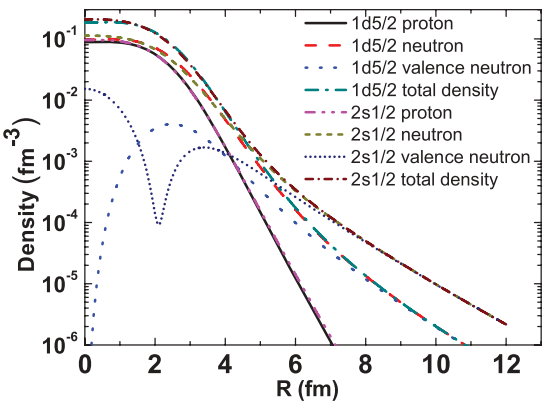

FIG. 1. (Color online) The proton, neutron, valence neutron, and total density distributions of ^{15}C for the valence neutron in the $1d5/2$ and $2s1/2$ states, respectively, by RMF calculations.

the proton, neutron, valence neutron, and total density distributions for two different configured ^{15}C projectiles, whose valence neutron is assigned to both $1d5/2$ and $2s1/2$ states, respectively. It can be seen that the valence neutron in the $2s1/2$ state has a longer tail than that in the $1d5/2$ state, whereas, the proton almost has the same density distributions for the two cases. The effect of the more extended valence neutron density distribution can be reflected by the nucleon-nucleon momentum-correlation function as shown below.

In our calculations, the initialization of ^{15}C is carefully controlled. The stability of the sampled ^{15}C projectiles is strictly checked by the time evolution in the mean field until 200 fm/c at zero temperature according to the average binding energies, root-mean-square (rms) radii, and density distributions of the neutron and proton. Eligible initialization samples should meet the following requirements until 200 fm/c: (a) The average binding energy needs to match with the experimental data; (b) the rms radius also needs to be in accordance with the RMF result; (c) the difference in the neutron tails between two kinds of ^{15}C projectiles should remain until 200 fm/c. To better imitate the input density from the RMF calculation and to reflect the structure effect, thousands of eligible initialized samples are accumulated for simulating collisions. The initialized samples of other C isotopes are prepared in a similar way as above.

Even with very elaborate initialization, the tail of the density in the QMD model cannot be reproduced very well compared with the RMF model since the wave function in the QMD model has a Gaussian form. However, the obvious differences in the neutron tails between two kinds of ^{15}C projectiles can remain stable enough, and thus, it can play the role of skin structure in the collisions. In the following, we present how the skin structure, expressed by different neutron density distributions in QMD, affects nucleon-nucleon momentum correlations.

The proton and neutron phase spaces of the ^{15}C + ^{12}C collisions at the freeze-out time generated by the IDQMD model is used as the input for the CRAB code. The obtained proton-proton, neutron-neutron, and proton-neutron momentum-correlation functions are shown in Fig. 2, respectively, where q denotes the relative momentum of the nucleon pair. As expected, C_{nn} and C_{pn} peak at small q, whereas, the proton-proton is anticorrelated at small q owing to the Coulomb potential and antisymmetrization. The peak of C_{pp} at 20 MeV/c is due to the s-partial wave of the proton-proton scattering, which strongly depends on the size of the emitting source. Our simulations pretty well reproduce the shape and height of C_{pp}, C_{nn}, and C_{pn} vs q compared with the experimental cases [14]. It can be seen that C_{nn} and C_{pn} are both largely reduced at small q because of the more extended neutron density distribution. In Fig. 2, the size of the emission source is mostly decided by projectilelike remnants since we adopt the impact parameter $b = 7$ to 8 fm and rapidity > 0. The rms radii of the proton, neutron, valence neutron, ^{14}C core, and ^{15}C by the RMF calculation and the experimental rms charge radius of ^{14}C are shown in Table I. The rms radii of initialized ^{15}C projectiles are required to meet the RMF calculated values. Although there is no available experimental rms radius of ^{15}C, the rms radius of the ^{14}C core reproduces

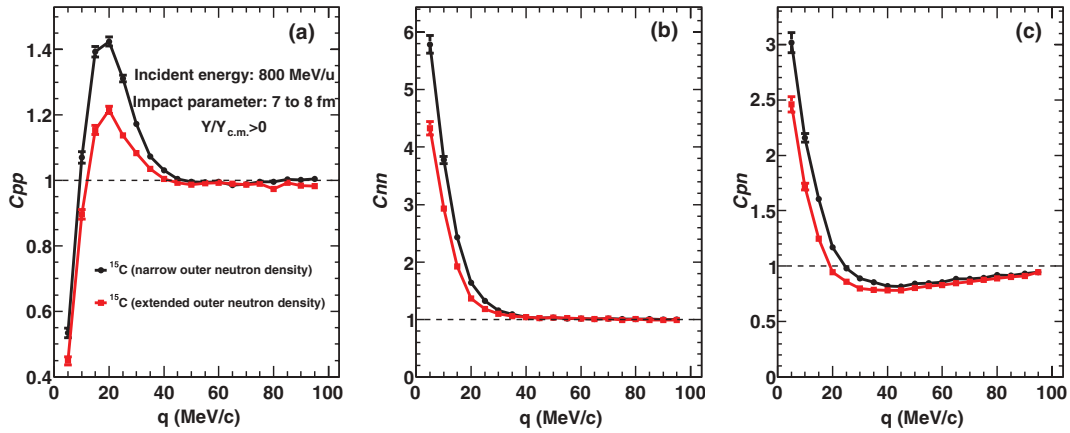

FIG. 2. (Color online) Proton-proton [C_{pp}, panel (a)], neutron-neutron [C_{nn}, panel (b)], and proton-neutron [C_{pn}, panel (c)] momentum-correlation functions as a function of relative momentum, which are calculated at an incident energy of 800 MeV/nucleon, an impact parameter of $b = 7$ to 8 fm, and selected nucleons with rapidity > 0. The circles and squares represent two different kinds of initialized ^{15}C-projectile-induced collisions where ^{15}C projectiles are sampled from two density outputs of the RMF model with valence neutrons in the $1d5/2$ and $2s1/2$ states, respectively. The dashed line is used to guide the eyes.

the experimental rms charge radius of ^{14}C quite well. The rms radii of ^{15}C do not have large differences for the two kinds of ^{15}C projectiles. However, the corresponding rms radii of the valence neutrons are 3.85 and 5.01 fm. Therefore, the strength of the momentum-correlation functions can, indeed, sensitively reflect the fine difference in the neutron density distribution. Although the density distributions of the proton for the two configured ^{15}C are almost the same (as seen in Fig. 1), C_{pp} still has large differences, which demonstrate that the proton density distribution has changed with proton emission. The density distributions of the neutrons and protons are coupling with each other during collisions.

The impact-parameter dependence of C_{pn} at the 800-MeV/nucleon incident energy for the two different kinds of initialized ^{15}C projectiles is shown in panel (a) of Fig. 3. The strength of correlation becomes decreasing with b up to 6.5 fm. In central collisions, emitted nucleons have stronger correlations between themselves because they come from one compact hot and dense region, which is consistent with previous Boltzmann-Uehling-Uhlenbeck [15,49] and IDQMD [16] results. In peripheral collisions with $b > 6.5$ fm, the rapid enhancement of C_{pn} reveals different collision dynamics from the central collisions. This is due to the fact that there is no bulk overlap region at the large impact parameter and only the outer nucleons of ^{15}C are scraped. They keep more initial structure information of the projectile. Thus, there exists a strong correlation among these nucleons. The difference in ^{15}C in the neutron density distribution, such as skin structure can be well revealed in peripheral collisions, whereas, the small difference in density is wiped away in the violent central and semiperipheral collisions.

How incident energy affects C_{pn} is represented in panel (b) of Fig. 3. The correlations for both cases increase from very low incident energy and then almost reach saturation above 300 MeV/nucleon. This is understandable due to the fact that increasing incident energies lead to more rapid collision processes, and there is a smaller space and time interval among emitting nucleons [16,49], which leads to stronger correlation. The apparent differences in C_{pn} exist for the two kinds of ^{15}C-induced collisions above the saturation energy. The saturation of C_{pn} at high incident energies and the large differences provide us with the proper entrance channel

TABLE I. The rms radii of initialized ^{15}C by RMF theory and experimental rms charge radius of ^{14}C. The rms radii of ^{15}C projectiles are initialized to match with the values in this table.

	Z (fm)	N (fm)	Valence N (fm)	^{14}C core (fm)	^{15}C (fm)	^{14}C exp. (Z) [48] (fm)
						2.50
^{15}C ($1d5/2$)	2.40	2.76	3.85	2.51	2.62	
^{15}C ($2s1/2$)	2.39	2.96	5.01	2.51	2.75	

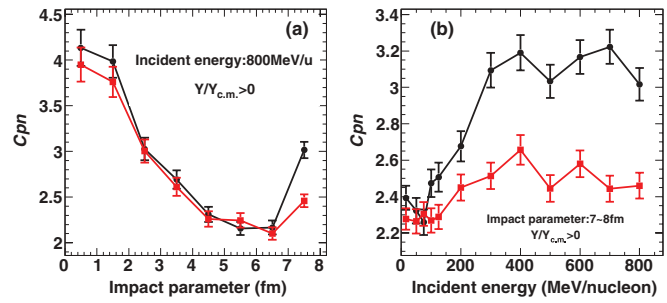

FIG. 3. (Color online) (a) C_{pn} strength at 5 MeV/c as a function of the impact parameter, which is calculated at an incident energy of 800 MeV/nucleon and selected nucleons with rapidity > 0; (b) C_{pn} strength at 5 MeV/c as a function of the incident energy, which is calculated at an impact parameter of $b = 7$ to 8 fm and selected nucleons with rapidity > 0. The symbols in both panels (a) and (b) have the same convention as in Fig. 2.

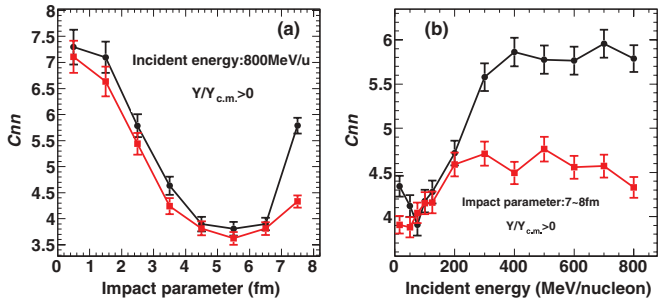

FIG. 4. (Color online) The same as Fig. 3 but for C_{nn}.

conditions to explore the relation between the initial structure and the final effect.

The impact-parameter and incident-energy dependences of C_{nn} are shown in panels (a) and (b) of Fig. 4, respectively. The tendency of C_{nn} is similar to C_{pn} for both impact parameter and energy dependences. The analogous results are also obtained for C_{pp} shown in Fig. 5.

The strength of C_{pn}, C_{nn}, and C_{pp} is mainly decided by the distance in phase space at the freeze-out time. Under specific entrance channel conditions (high energy and large impact parameter), the size of the phase space in the final state is consistent with the initial size of the ^{15}C projectile, which largely depends on the neutron-skin structure. This can be seen from Fig. 6, which shows the impact-parameter dependences of the rms radii in coordinate and momentum space. The size of the phase space decreases with the increase in impact parameter. The more extended neutron skin leads to larger rms radii of the coordinate and momentum in the final state for peripheral collisions at 800 MeV/nucleon, which results in a smaller correlation in the HBT method. However, rms radii do not have differences between the two kinds of ^{15}C-induced reactions in the central and semiperipheral collisions because the only difference in the outer neutron is covered in the violent collisions. Therefore, the physical picture of the phase-space size is consistent with the impact-parameter dependences of C_{pn}, C_{nn}, and C_{pp}. The excitation function of the rms radii of the phase space in peripheral collisions shown in Fig. 7 gradually become saturated at high incident energies, which can explain the saturation of the correlations in panel (b) of Figs. 3–5.

The space-time extent of the emission source for different particles can be extracted from the shape and height of C_{pp}, C_{nn}, and C_{pn} for ^{15}C projectiles with and without neutron

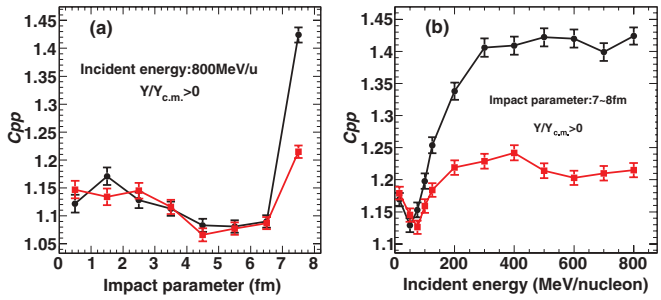

FIG. 5. (Color online) The same as Fig. 3 but for C_{pp}.

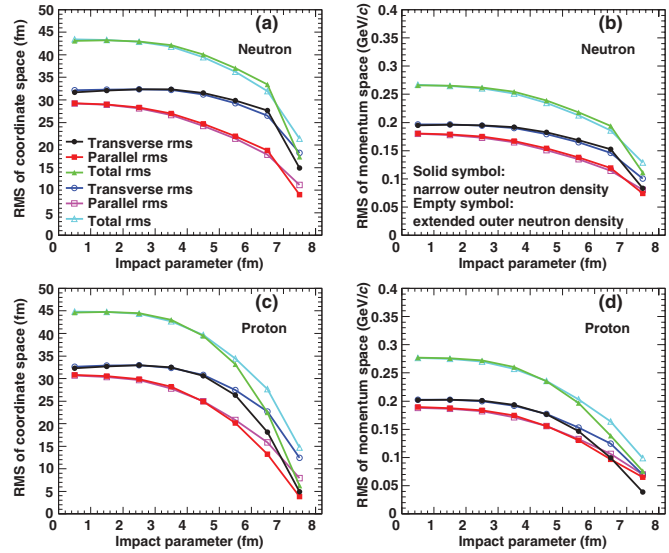

FIG. 6. (Color online) Root-mean square of coordinate- [panels (a) and (c)] and momentum- [panels (b) and (d)] space distributions in the center-of-mass reference frame as a function of the impact parameter at an incident energy of 800 MeV/nucleon and rapidity >0 for the neutrons [panels (a) and (b)] and protons [panels (c) and (d)], respectively. The solid (empty) circles, squares, and triangles represent transverse, parallel, and total rms radii, respectively, for ^{15}C-projectile-induced collisions, where ^{15}C projectiles are sampled from two density outputs of the RMF model with valence neutrons in the $1d5/2$ and $2s1/2$ states, respectively.

skins. The angle-averaged Koonin-Pratt formula can be written as [4,50]

$$R(q) = 4\pi \int r^2 dr\, K(q,r) S(r), \tag{5}$$

where $S(r)$ is the isotropic source function, which stands for the probability distribution of emitting a pair of nucleons at relative distance r. $K(q,r)$ is the angle-averaged kernel function obtained from the radial part of the two-nucleon relative wave function. If we assume $S(r)$ has a simple Gaussian form

$$S(r) = \frac{1}{(2\pi)^{3/2}\sigma^3} \exp\left(-\frac{r^2}{2\sigma^2}\right), \tag{6}$$

where σ describes the spatial distribution of the nucleons' emitting location and the rms radius of the Gaussian emission source equals $\sqrt{3}\sigma$. The Gaussian source method is used to fit the correlation functions (C_{pp}, C_{nn}, and C_{pn}) for two kinds of ^{15}C-induced collisions. Panel (d) of Fig. 8 represents the variance between the IDQMD and the Gaussian source correlations as a function of the rms radius of the Gaussian source. Then, the best fitting is judged by the variance, and the rms radii obtained are shown in panels (a)–(c), respectively. We get the same Gaussian source size from C_{nn} and C_{pn}. The emission source size of projectiles with skin structures is about 20% larger than that of projectiles without skin structures for C_{nn} and C_{pn}. The source size from C_{pp} is smaller than that from C_{nn} and C_{pn} for both kinds of ^{15}C projectiles. By comparing with the initialized neutron distribution shown in Fig. 1 and Table I, we can conclude that the initial structure information of

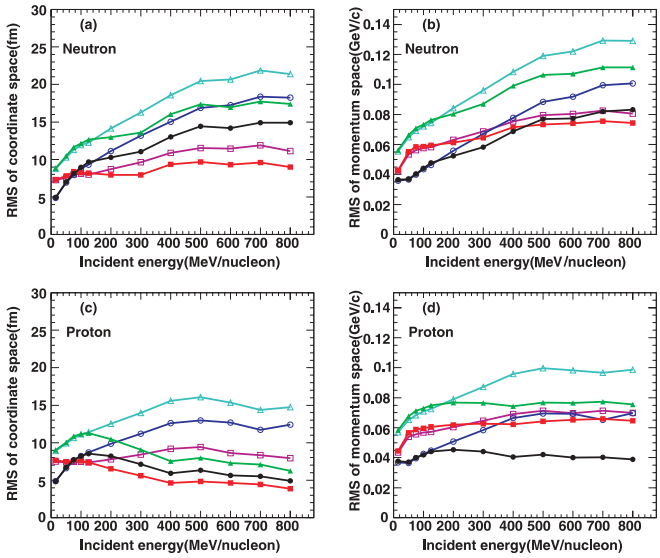

FIG. 7. (Color online) Root-mean square of coordinate- [panels (a) and (c)] and momentum- [panels (b) and (d)] space distributions in the center-of-mass reference frame as a function of the incident energy with an impact parameter of $b = 7$ to 8 fm and rapidity > 0 for the neutrons [panels (a) and (b)] and protons [panels (c) and (d)], respectively. The symbols have the same convention as in Fig. 6.

the neutron skin and the size of the projectile are kept until the final state. The size of the proton emission source is different for the two kinds of ^{15}C projectiles, although the initial density distribution of the proton is the same. The size is about 15% larger for projectiles with the neutron skin, which proves that

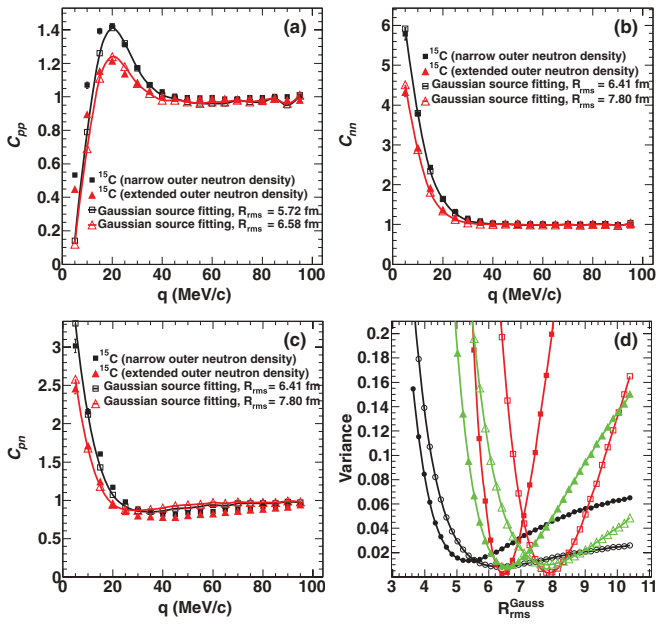

FIG. 8. (Color online) Gaussian source fitting for C_{pp} [panel (a)], C_{nn} [panel (b)], C_{pn} [panel (c)], and the variance between the IDQMD + CRAB correlation and the Gaussian source correlation as a function of the rms radius of the Gaussian source [panel (d)]. The entrance channel conditions at the 800-MeV/nucleon bombarding energy and the impact parameter with $b = 7$ to 8 fm are used, and the nucleons with rapidity > 0 in the final state are chosen.

the proton density distribution is disturbed through interaction with neutrons even in very peripheral collisions.

The size of the emission source extracted above is under the hypothesis that the nucleon is expressed by a point particle. However, in the QMD model, the nucleon wave function has a Gaussian form in coordinate and momentum space. The true distribution of the source is the convolution of the distribution of the wave-packet center with the Gaussian density distribution of a single nucleon. In Refs. [51,52], the relation between the rms radius of the freeze-out points $\langle r(t)^2\rangle^{1/2}$ and the variance of the source and wave function is obtained by assuming that a chaotic Gaussian source has formed in the collision without a correlation between coordinate and momentum space,

$$\langle r(t)^2\rangle^{1/2} = \sqrt{3(A+L)}, \tag{7}$$

where A is the variance of the chaotic emission source with the Gaussian form and L is the square of the width of the Gaussian wave packet in the QMD model with a value of 2.16 fm^2 in our calculations. Now, with a finite width modification of the Gaussian wave packet, we then get a smaller rms radius of the emission source: $\sqrt{3A} = \sqrt{3(\sigma^2 - L)}$. For example, the rms radii from C_{pp} are 5.12 and 6.07 fm for ^{15}C projectiles with and without neutron skins, respectively. The rms radii from both C_{nn} and C_{nn} have the same value: 5.88 and 7.37 fm, respectively.

We also study the systematical dependence of the momentum correlation on other C-isotope-induced collisions. Figure 9 shows the strength of C_{pp} at 20 MeV/c for $^{12-16}$C + ^{12}C systems. The collisions are compared at the same reduced parameter range: 0.875–1.0. Four kinds of ^{15}C projectiles

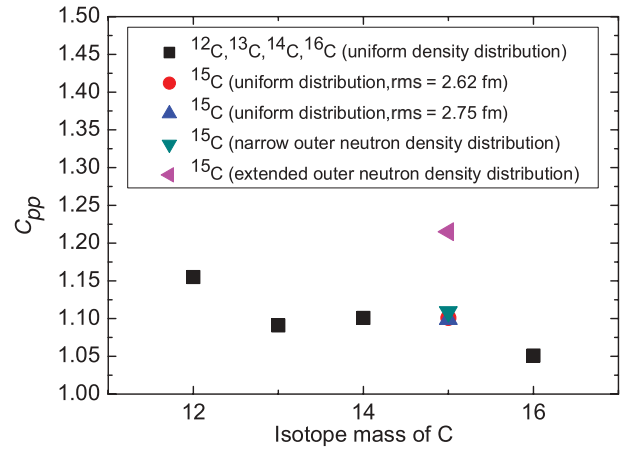

FIG. 9. (Color online) Dependence of C_{pp} (strength of C_{pp} at 20 MeV/c) on C-isotope- ($^{12-16}$C) induced collisions. Different collision systems are compared with the same reduced impact-parameter range: 0.875–1.0, and only protons with rapidity > 0 are used to calculate the momentum-correlation function. Nucleons of ^{12,13,14,16}C are sampled from the uniform density distribution. We construct four kinds of ^{15}C projectiles: Two of them are sampled from the two RMF densities shown in Fig. 1, respectively, and the other two are sampled from the uniform distribution with two different sizes, which correspond to the sizes of the $1d5/2$ and $2s1/2$ states in the RMF model, respectively.

are constructed. The other two kinds of ^{15}C projectiles are sampled from uniform density distributions besides the sampling from the RMF discussed above. Nucleons also have uniform distribution in ^{12}C, ^{13}C, ^{14}C, and ^{16}C projectiles. The total systematical tendency of the mass dependence of C_{pp} is decreasing except for projectiles with neutron-skin structures, which can be interpreted as follows: Although they are simulated at the same reduced impact parameter, $^{12}\mathrm{C} + ^{12}\mathrm{C}$ collisions have a smaller emission source as compared with $^{16}\mathrm{C} + ^{12}\mathrm{C}$ collisions. The correlation for projectiles with neutron skins is stronger than in other cases. This is because the outer density distribution is more extended due to the neutron skin, and then, it results in a smaller overlap zone between the projectile and the target for the same reduced impact parameter at peripheral collisions. Therefore, the proton-protons have a stronger correlation due to the fact that they come from one compact projectilelike remnant, which is obviously different from the case without a skin structure.

IV. SUMMARY

The very small nucleon separation energy of the last nucleon and the suddenly increased radius compared with its neighboring isotopes are the two main features of the exotic halo nucleus. The HBT method has been used to study the relationship between momentum correlation and single-nucleon separation energy several years before. In this paper, we systematically investigated how the density distribution of the valence neutron in the one-neutron-halo candidate ^{15}C affected the strength of the nucleon-nucleon momentum-correlation function. Specifically, two kinds of ^{15}C projectiles were sampled from two different density outputs of the RMF model, respectively. The difference in the outer neutron density distribution between two kinds of initialized ^{15}C samples can be viewed as a neutron-skin structure in the IDQMD simulation. The more extended density distribution due to the outer neutron in the projectile results in the larger and hot emission source, which leads to a larger size of phase space in the final state and then corresponds to a weaker correlation. The energy and impact-parameter dependences show that the nucleon-nucleon momentum-correlation function is a very sensitive observable of the density distribution of the valence neutron at high-energy and peripheral collisions. Therefore, the momentum-correlation function at the high bombarding energy and large impact parameter can serve as a new potential probe to diagnose the exotic structures, such as skin and halo, besides the traditional measurements of the total reaction cross section and momentum distribution.

ACKNOWLEDGMENTS

We wish to thank Professor S. Pratt for providing the CRAB code, which was used to construct the momentum-correlation function from the phase-space data. This work was partially supported by the National Natural Science Foundation of China under Contracts No. 11175231, No. 11035009, No. 11005140, No. 10979074, No. 10875160, No. 10805067, and No. 10975174, the Major State Basic Research Development Program in China under Contract No. 2013CB834405 and the Knowledge Innovation Project of the Chinese Academy of Sciences under Grant No. KJCX2-EW-N01.

[1] R. Hanbury Brown and R. Q. Twiss, Nature (London) **178**, 1046 (1956).
[2] G. Goldhaber *et al.*, Phys. Rev. **120**, 300 (1960).
[3] S. Pratt and M. B. Tsang, Phys. Rev. C **36**, 2390 (1987).
[4] S. E. Koonin, Phys. Lett. B 70, 43 (1977).
[5] S. Pratt, Phys. Rev. Lett. **53**, 1219 (1984).
[6] J. P. Sullivan *et al.*, Phys. Rev. Lett. **70**, 3000 (1993).
[7] D. H. Boal *et al.*, Rev. Mod. Phys. **62**, 553 (1990).
[8] W. Bauer, C. K. Gelbke, and S. Pratt, Annu. Rev. Nucl. Part. Sci. **42**, 77 (1992).
[9] U. Heinz *et al.*, Annu. Rev. Nucl. Part. Sci. **49**, 529 (1999).
[10] U. A. Wiedemann *et al.*, Phys. Rep. **319**, 145 (1999).
[11] W. D. Oliver *et al.*, Science **284**, 299 (1999).
[12] M. Henny *et al.*, Science **284**, 296 (1999).
[13] R. Ghetti *et al.*, Phys. Rev. Lett. **91**, 092701 (2003).
[14] G. Verde *et al.*, Eur. Phys. J. A **30**, 81 (2006).
[15] W. G. Gong, W. Bauer, C. K. Gelbke, and S. Pratt, Phys. Rev. C **43**, 781 (1991).
[16] Y. G. Ma *et al.*, Phys. Rev. C **73**, 014604 (2006).
[17] N. Colonna, D. R. Bowman, L. Celano, G. D'Erasmo, E. M. Fiore, L. Fiore, A. Pantaleo, V. Paticchio, G. Tagliente, and S. Pratt, Phys. Rev. Lett. **75**, 4190 (1995).
[18] R. Ghetti *et al.*, Phys. Rev. C **69**, 031605(R) (2004).
[19] L. W. Chen, V. Greco, C. M. Ko, and B. A. Li, Phys. Rev. Lett. **90**, 162701 (2003).
[20] K. Ieki *et al.*, Phys. Rev. Lett. **70**, 730 (1993).
[21] F. M. Marqués *et al.*, Phys. Lett. B **476**, 219 (2000).
[22] F. M. Marqués *et al.*, Phys. Rev. C **64**, 061301(R) (2001).
[23] M. T. Yamashita, T. Frederico, and L. Tomio, Phys. Rev. C **72**, 011601(R) (2005).
[24] M. Petrascu *et al.*, Phys. Rev. C **69**, 011602(R) (2004).
[25] M. Petrascu *et al.*, Nucl. Phys. A **790**, 235c (2007).
[26] Y. B. Wei *et al.*, Phys. Lett. B **586**, 225 (2004).
[27] Y. B. Wei *et al.*, J. Phys. G **30**, 2019 (2004).
[28] Y. G. Ma *et al.*, Nucl. Phys. A **790**, 299c (2007).
[29] I. Tanihata *et al.*, Phys. Lett. B 160, 380 (1985).
[30] T. Kobayashi, O. Yamakawa, K. Omata, K. Sugimoto, T. Shimoda, N. Takahashi, and I. Tanihata, Phys. Rev. Lett. **60**, 2599 (1988).
[31] P. Zhou *et al.*, Int. J. Mod. Phys. E **19**, 957 (2010).
[32] X. Y. Sun *et al.*, Int. J. Mod. Phys. E **19**, 1823 (2010).
[33] G. Audi, A. H. Wapstra, and C. Thibault, Nucl. Phys. A **729**, 337 (2003).
[34] D. Bazin *et al.*, Phys. Rev. C **57**, 2156 (1998).
[35] D. Q. Fang *et al.*, Phys. Rev. C **69**, 034613 (2004).
[36] G. Murillo, S. Sen, and S. E. Darben, Nucl. Phys. A **579**, 125 (1994).
[37] A. Ozawa, T. Suzuki, and I. Tanihata, Nucl. Phys. A **693**, 32 (2001).
[38] D. Q. Fang *et al.*, Phys. Rev. C **61**, 064311 (2000).
[39] A. Ozawa *et al.*, Nucl. Phys. A **608**, 63 (1996).
[40] S. Pratt *et al.*, Nucl. Phys. A **566**, 103c (1994).

[41] J. Aichelin, A. Rosenhauer, G. Peilert, H. Stoecker, and W. Greiner, Phys. Rev. Lett. **58**, 1926 (1987).
[42] J. Aichelin, Phys. Rep. **202**, 233 (1991).
[43] G. Peilert, H. Stöcker, W. Greiner, A. Rosenhauer, A. Bohnet, and J. Aichelin, Phys. Rev. C **39**, 1402 (1989).
[44] T. Z. Yan *et al*., Phys. Lett. B **638**, 50 (2006).
[45] X. G. Cao, G. Q. Zhang, X. Z. Cai, Y. G. Ma, W. Guo, J. G. Chen, W. D. Tian, D. Q. Fang, and H. W. Wang, Phys. Rev. C **81**, 061603(R) (2010).
[46] G. Q. Zhang, Y. G. Ma, X. G. Cao, and C. L. Zhou, Phys. Rev. C **83**, 064607 (2011).
[47] G. Q. Zhang, Y. G. Ma, X. G. Cao, C. L. Zhou, X. Z. Cai, D. Q. Fang, W. D. Tian, and H. W. Wang, Phys. Rev. C **84**, 034612 (2011).
[48] I. Angeli, At. Data Nucl. Data Tables **87**, 185 (2004).
[49] L. W. Chen, V. Greco, C. M. Ko, and B. A. Li, Phys. Rev. C **68**, 014605 (2003).
[50] G. Verde, D. A. Brown, P. Danielewicz, C. K. Gelbke, W. G. Lynch, and M. B. Tsang, Phys. Rev. C **65**, 054609 (2002).
[51] J. Aichelin, Nucl. Phys. A **617**, 510 (1997).
[52] F. Gastineau and J. Aichelin, Phys. Rev. C **65**, 014901 (2001).